Multifunctional nanocarriers of Fe$_3$O$_4$@PLA-PEG/curcumin for MRI, magnetic hyperthermia and drug delivery

Phan Quoc Thong[‡,1,2], Le Thi Thu Huong[‡,1,3] (iD), Nguyen Dac Tu[4], Hoang Thi My Nhung[4] (iD), Lam Khanh[5], Do Hung Manh[1] (iD), Pham Hong Nam[1,6] (iD), Nguyen Xuan Phuc*[,1,7] (iD), Javier Alonso[8,9] (iD), Ju Qiao[10], Srinivas Sridhar[10], Ha Phuong Thu[1] (iD), Manh Huong Phan**[,9] (iD) & Nguyen Thi Kim Thanh***[,11,12] (iD)

[1]Institute of Materials Science, Vietnam Academy of Science and Technology, 18 Hoang Quoc Viet, Cau Giay, Hanoi, 11355, Vietnam
[2]University of Khanh Hoa, 1 Nguyen Chanh, Nha Trang, 57100, Vietnam
[3]Faculty of Natural Resources and Environment, Vietnam National University of Agriculture, Trau Quy, Gia Lam, Hanoi, 12400, Vietnam
[4]Hanoi University of Science, Vietnam National University, 334 Nguyen Trai, Hanoi, 11400, Vietnam
[5]108 Military Central Hospital, 1 Tran Hung Dao, Hanoi, 11000, Vietnam
[6]Graduate University of Science & Technology, Vietnam Academy of Science and Technology, 18 Hoang Quoc Viet, Cau Giay, Hanoi, 12400, Vietnam
[7]Duy Tan University, 3 Quang Trung, Danang, 50300, Vietnam
[8]Department of CITIMAC, Universidad de Cantabria, Santander, 39005, Spain
[9]Department of Physics, University of South Florida, Tampa, FL 33620, USA
[10]Department of Physics, Bioengineering & Chemical Engineering, Northeastern University, Boston, MA 02115, USA
[11]Biophysics Group, Department of Physics and Astronomy, University College London, Gower Street, WC1E 6BT, London
[12]UCL Healthcare Biomagnetics & Nanomaterials Laboratories, 21 Albemarle Street, London W1S 4BS, UK
*Author for correspondence: phucnx@ims.vast.ac.vn
**Author for correspondence: phanm@usf.edu
***Author for correspondence: ntk.thanh@ucl.ac.uk
‡LTT Huong and PQ Thong contributed equally to the manuscript

Background: Despite medicinal advances, cancer is still a big problem requiring better diagnostic and treatment tools. Magnetic nanoparticle (MNP)-based nanosystems for multiple-purpose applications were developed for these unmet needs. **Methods:** This study fabricated novel trifunctional MNPs of Fe$_3$O$_4$@PLA-PEG for drug release, MRI and magnetic fluid hyperthermia. **Result:** The MNPs provided a significant loading of curcumin (∼11%) with controllable release ability, a high specific absorption rate of 82.2 W/g and significantly increased transverse relaxivity (r_2 = 364.75 mM^{-1} s^{-1}). The *in vivo* study confirmed that the MNPs enhanced MRI contrast in tumor observation and low-field magnetic fluid hyperthermia could effectively reduce the tumor size in mice bearing sarcoma 180. **Conclusion:** The nanocarrier has potential for drug release, cancer treatment monitoring and therapy.

Plain language summary: In this study, the authors designed and fabricated novel magnetic trifunctional nanoparticles of Fe$_3$O$_4$@PLA-PEG. The 8.5 nm Fe$_3$O$_4$ core was covered with the polymeric matrix of PLA-PEG to encapsulate an anticancer agent of curcumin at a content of about 11%. Curcumin release from the nanoparticles (NPs) could be controlled by applying a remote alternating magnetic field. The NPs enhanced MRI contrast, which allowed the authors to better distinguish the tumor and surroundings in MR images, which would help monitor treatment. The heat that NPs generated when applied to a field at low intensity could effectively reduce the tumor size in mice bearing sarcoma 180. The nanocarrier, therefore, has potential for cancer treatment monitoring and drug release conjuvant with magnetic hyperthermia therapy.

Graphical abstract:
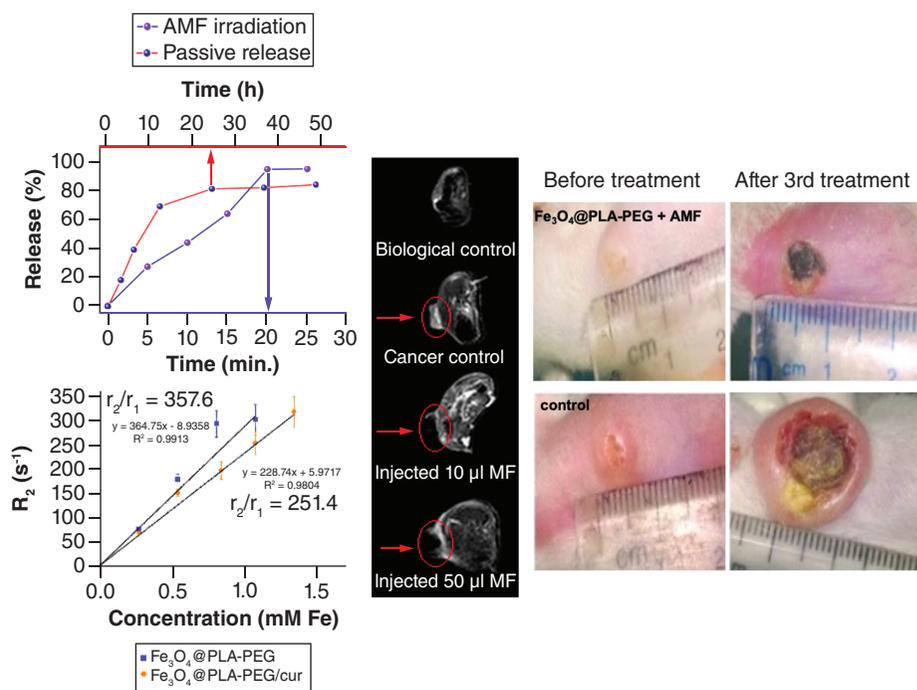
Nanoparticles (NPs) are finding an increasing number and variety of applications in biomedicine, including detection, imaging and therapeutic treatment [1–7]. In general, these NPs consist of a solid, inorganic core encapsulated by a shell, normally of soft matter, and frequently including functional molecules of a drug or targeting agent [2].

Among the core materials, magnetic nanoparticles (MNPs) are leading candidates for biomedical applications, owing to their superparamagnetic properties [7–14]. For instance, MNPs can experience a force in an applied gradient magnetic field in bioseparation or drug delivery [15]. When localized in a biological environment, MNPs can create inhomogeneities of the local magnetic field, thus influencing the magnetic relaxation rate of water-containing tissues. That is why they have been intensively investigated and are now used as agents for MRI contrast enhancement in clinical diagnostics [16–21]. Probably, one of the most attractive properties of MNPs is the so-called magnetic fluid hyperthermia (MFH), which is based on their capability to adsorb energy from an alternating magnetic field (AMF) to generate heat via their Néel and/or Brownian relaxation dissipation [11,22]. When inserted into tumor tissues, MNPs can kill cancer cells by increasing the local temperature, because cancer cells show stronger thermal cytotoxicity than normal cells [23]. Therefore, MNPs have been intensively studied for their use as potential MFH agents in cancer treatment [24–26]. Among the MNPs, Fe_3O_4 MNPs have been the most intensively studied thanks to their suitable magnetic properties, biodegradability, biocompatibility and ability to be functionalized and drug encapsulated [27].

Functionalization of MNPs is an important step; with a biocompatible coating layer, not only do the MNPs become stabilized and protected from further oxidation but in many cases this process can also impact the magnetic properties of the core [28–31]. Several studies on iron oxides have shown that due to the interaction of the coating material with the NP surface, the magnetization might be decreased or increased depending on the ligands used, as well as the encapsulation procedure [28,30]. Regarding the coating material, beyond silica and carbon, most of the materials that have been studied are various types of polymers [10,14,32–36]. Recent studies have shown that using copolymer is very effective for encapsulating MNPs to disperse them in water [32,33,35]. A hydrophobic monomer such as polylactic acid (PLA) can anchor well on iron oxide NPs, whereas a hydrophilic monomer such as PEG can exhibit a good dispersibility in water. To additionally make the magnetic nanocarrier capable of delivering chemical therapy, several molecular drugs, including folic acid, doxorubicin, dopamine and curcumin have been loaded onto MNPs [37–42]. Among these drugs, curcumin can exhibit great pharmacological potential, including anti-inflammatory, antioxidant, antiproliferative and chemosensitizing, cell cycle arrest potential, and can display apoptotic potential against various cancer cells such as colorectal, breast, pancreatic and colon cancers, there-

fore renders it great potential in cancer prevention and therapy. Notably, the IC$_{50}$ of curcumin in healthy cells is significantly higher than that in cancer cells [43]. It was used in this study as a model for drug delivery and release of nanocarriers.

The potential of using an Fe$_3$O$_4$-based nanocarrier as both a drug release and hyperthermia agent has been reported in several works [40,41]. MRI and MFH are important on their own [44–47] or are sometimes found in combination [48]. However, few reports have shown experimentally the fabrication of a nanocarrier simultaneously demonstrating the optimal performance of MRI, drug release and MFH. In 2011, although doxorubicin-loaded γ-Fe$_2$O$_3$ NPs were evaluated for their ability in diagnosis and hyperthermia, no *in vivo* experiment was carried out [49].

Saturation magnetization (M_s) is well known to be one of the most important factors in all the biomedical applications of MNPs. The magnetic force, F, in manipulation application is defined as linearly proportional to M_s [15]. The relaxation rate (R_2) in MRI is approximately proportional to $(M_s \times V_{NPs})^2$, where V_{NPs} is the volume of the NPs [17,18]. The specific absorption rate (SAR) is dependent on magnetization [50] and magnetic anisotropy [51–53]. Therefore, M_s should be carefully evaluated for the applications of MRI and MFH. In addition to M_s of the MNPs, the field strength (H) and frequency (f) of the magnetic field used should also be considered in *in vivo* MFH experiments. There are some criteria for H×f product for *in vivo* MFH. For example, the Atkinson–Brezovich criterion requires the H×f product to be lower than 5×10^8 A/(m·s) [54]. However, according to the Dutz–Hergt criterion, this number could be ten-times larger to obtain safety for *in vivo* experiments [55]. Most authors used a higher field than the Atkinson–Brezovich criterion, while some reports even used a much higher field than the Dutz–Hergt criterion in their studies [56].

In this study, the authors aimed to fabricate functionalized magnetic Fe$_3$O$_4$ NPs using amphiphilic PLA-PEG copolymer as a biodegradable coating material. A thorough chemical and physical characterization, including magnetization, magnetic heating performance and nuclear relaxation rate, was carried out. In addition, *in vivo* MRI and MFH tumor treatment experiments were carried out to show the effectiveness of the nanocarriers. Utilization of the NPs as the carriers for curcumin, a thermally stable anticancer drug [57] with control release ability, is presented to show the true multifunctional potential of the fabricated biomedical nanocarrier. The novelty of this study arises from the trifunctions of the MNPs and the lower field used in the *in vivo* MFH-mediated drug-release experiments than those in other studies using Fe$_3$O$_4$-based NPs.

Materials & methods

Materials

Lactic acid, PEG 2000 and tin(II) 2-ethylhexanoate (Sn(Oct)$_2$) were purchased from Sigma (MO, USA); FeCl$_3$, FeCl$_2$·4H$_2$O, NH$_4$OH, C$_7$H$_8$, dichloromethane (DCM), CH$_3$OH and C$_2$H$_5$OH and phosphate-buffered saline (PBS; pH 7.4) were purchased from Merck (Darmstadt, Germany); curcumin was provided by PharmaGenica Healthcare Pvt Ltd (Bengaluru, India). Distilled water was used for all experiments.

Synthesis & characterization of chemical, structural & basic magnetic properties

PLA-PEG copolymer was synthesized by ring-opening polymerization reaction between lactic acid and PEG in the presence of catalyst Sn(Oct)$_2$ [58]. PLA-PEG copolymer (molecular weight of 10 kDa) was dissolved in DCM (1 mg/ml) and stirred for 24 h; then H$_2$O was added to form a mixture, which was stirred for another 24 h to disperse PLA-PEG copolymer from DCM to H$_2$O. DCM solvent was then evaporated to obtain a dispersion of PLA-PEG copolymer in H$_2$O (1 mg/ml).

Fe$_3$O$_4$ NPs were synthesized by the coprecipitation method (based on previous work) [59]. Complex Fe$_3$O$_4$@PLA-PEG NPs were fabricated from suspensions of readily fabricated Fe$_3$O$_4$ and PLA-PEG NPs through the procedure described in Thong *et al.* [60]. In brief, 20 ml of Fe$_3$O$_4$ NPs dispersed in water at the concentration of 3 mg/ml was slowly dropped into 20 ml of 0.3 mg/ml PLA-PEG copolymer solution and stirred for 24 h to obtain Fe$_3$O$_4$@PLA-PEG NPs (suspension A). The suspension was stored at room temperature (22–32°C) for more than 90 days and no aggregation was observed by eye. To get a more concentrated suspension, suspension A was introduced to a rotary vacuum evaporator. To prepare Fe$_3$O$_4$@PLA-PEG/Cur, 1 ml of 4 mg/ml curcumin dissolved in C$_2$H$_5$OH was slowly dropped into 10 ml of suspension A and stirred for 48 h, and then ethanol was allowed to evaporate to obtain Fe$_3$O$_4$@PLA-PEG/Cur aqueous suspensions.

Crystal structure was determined by x-ray diffraction (XRD) technique in D8 Advance Bruker equipment. The morphology, size and size distribution of NPs were characterized by a Hitachi S-4800 field emission–scanning

electron microscopy (Hitachi S-4800) and transmission electron microscopy (TEM; JEOL JEM 1010), while the hydrodynamic diameter of the nanocarriers was determined from dynamic light scattering measurements using a Nano-Zetasizer (Malvern, Malvern, UK). Chemical bonding of the components in the NPs was verified by Shimadzu Prestige-21 Fourier-transform infrared spectroscopy. The mass contribution of PLA-PEG and curcumin on NPs was determined by thermogravimetric analysis (TGA) with a Shimadzu DTG-60H. Hysteresis loops at room temperature up to 880 kA/m were measured by a homemade vibrating sample magnetometer.

MRI characterization

The longitudinal and transverse relaxation rates, $R_1 = 1/T_1$ and $R_2 = 1/T_2$, respectively, were measured on a 7 T Bruker Biospec using a quadrature 300 MHz, 30 mm mouse coil (Animal Imaging Research, LLC, MA, USA). More details about the MRI measurement can be found in the Electronic Supplementary Information (ESI).

The longitudinal and transverse relaxivities, r_1 and r_2, of the nanocarriers were determined, using Equation 1, as a proportional factor from the linear dependencies of the corresponding relaxation rates on iron concentration, C:

$$R_{1,2} = R_{1,2}^0 + r_{1,2} \times C \qquad \text{(Equation 1)}$$

where $R_{1,2}^0$ is the relaxation rate of the liquid [30].

MFH measurements

Experiments to determine the MFH effect of the nanosystems were carried out on an RDO induction generator (RDO Induction, NJ, USA) of 5 kW at field amplitudes $H \leq 8000$ A/m and frequency $f = 178$ kHz. This equipment was also used for the controlled drug-release experiment.

The heating curves of the ferrofluids were measured to determine the SAR, according to Equation 2:

$$SAR = C_p \times \left(\frac{m_t}{m_{NPs}} \right) \times \frac{dT}{dt} \qquad \text{(Equation 2)}$$

where C_p is the specific heat of the liquid (4.186 J/g°C for water), m_l and m_{NPs} are the corresponding mass of the liquid and nanocarrier and dT/dt is the initial rate of temperature increase [61].

Temperature change measurements were performed for ferrofluid samples at the concentration of 1.63 mg_{Fe}/ml at the volume of 1.0 ml. Distilled water was used as the only suspension solvent for the measurements.

In vitro curcumin release

For the passive curcumin release procedure, 10 mg of Fe_3O_4@PLA-PEG/Cur MNPs were dispersed in 30 ml PBS. The dispersion was incubated in a water bath at 37°C for 48 h. At desired time intervals (4 h for the first 12 h and 12 h for the remaining time), a 2 ml sample was withdrawn and replaced with an equal volume of the fresh release medium (PBS, pH 7.4). The curcumin concentration in each taken sample was determined by UV-VIS spectroscopy.

For the first controlled release experiment series by MFH, five samples, each containing 1 ml aliquot of Fe_3O_4@PLA-PEG/Cur aqueous solution, were excited by the same AMF at a frequency $f = 178$ kHz, $H = 5040$ A/m, starting from the same temperature of 25°C, and ending after a certain period (5, 10, 15, 20 and 25 min). Another series of experiments were set up with the AMF stimulation at different magnetic fields, at a frequency $f = 178$ kHz, and amplitudes varying from 3600 to 5040 A/m until the sample temperature reached 37°C or 45°C. After MFH treatment, the concentration of curcumin released by AFM stimulation from the samples was determined by UV-Vis spectroscopy.

Animal experiments

In vivo MRI experiments

MRI monitoring experiments were conducted in sarcoma-bearing Swiss mice. Ten days after tumor incubation, three mice with similar tumor sizes and one normal mouse (with no tumor) were selected for MRI investigation. The mice were numbered as follows:

- Mouse A: normal mouse as biological control;
- Mouse B: noninjected mouse with tumor, cancer control;

- Mouse C: mouse with tumor, injected with 10 µl of 5 mg/ml Fe₃O₄@PLA-PEG ferrofluid directly into the tumor;
- Mouse D: mouse with tumor, injected with 50 µl of 5 mg/ml Fe₃O₄@PLA-PEG ferrofluid directly into the tumor.

Then all the mice were anesthetized with 65 µl of 0.25 mg/ml thiopental (injected through a tail vein). The mice were then taken for imaging in a Philips Gyroscan 3.0 T MRI (Philips, Eindhoven, The Netherlands) at 0, 15, 30, 45 and 60 min after injecting the magnetic fluid into the tumor. Image acquisition was performed in the spin echo mode with a repetition time of 3000 ms and an echo time of 80 ms.

Similar experiments were conducted with other four mice with 5-day-old tumors (among which, one mouse was the biological control) in order to investigate the ability of early tumor diagnosis based on MRI.

In vivo tumor treatment with MFH

The effectiveness of the fabricated nanocarriers in hyperthermia was investigated via the capability of thermal therapy of sarcoma 180, a heterogeneous tumor that is easily directly injected. The animal experiments were performed on mice using Fe₃O₄@PLA-PEG ferrofluid of 5 mg/ml concentration of Fe₃O₄ in water at tumor volume-dependent doses.

Two series of experiments were carried out on Swiss mice with solid tumors of sarcoma 180 were incubated subcutaneously at the stomach site for 5 days and 10 days before MFH experiments. Each experimental series consisted of four groups:

- Group 1: 6 noninjected and nonirradiated mice as a control;
- Group 2: 6 noninjected mice with AMF irradiation;
- Group 3: 6 mice injected with Fe₃O₄@PLA-PEG and without AMF irradiation;
- Group 4: 6 mice injected with Fe₃O₄@PLA-PEG and subjected to AMF.

The treatment efficiency was described by observation of tumor volume V, which was calculated using Equation 3:

$$V = 0.5 \times a \times b^2 \, (\text{cm}^3)$$

(Equation 3)

where a is tumor length and b is tumor width [62].

A dose of 500 µg ferrofluid/cm³ tumor was injected directly into the tumor site. A field of 5040 A/m and 178 kHz was applied for 40 min, starting at 30 min after the injection of Fe₃O₄@PLA-PEG/Cur NPs into the mice (similar to the authors' previous protocol [42]). Each therapy consisted of three sessions of AMF treatment, with a 48 h break in between.

Results

Characterization

A proposed structure of the NPs is shown in Supplementary Figure 1 in ESI. Detailed characterizations of Fe₃O₄@PLA-PEG and Fe₃O₄@PLA-PEG/Cur were carried out in a previous work [60]. Herein, the authors present only the crucial properties of the systems. First, XRD patterns of all three samples (Fe₃O₄, Fe₃O₄@PLA-PEG and Fe₃O₄@PLA-PEG/Cur) showed six clearly defined diffraction peaks, very similar, independently of the sample, which correspond to the typical (200), (311), (400), (422), (511) and (440) diffraction peaks of spinel structure (Supplementary Figure 2 in ESI). This suggests that the formation of multicompositional NPs, Fe₃O₄@PLA-PEG and Fe₃O₄@PLA-PEG/Cur, does not affect the crystal structure of Fe₃O₄. This may result in the conservation of magnetic properties of the system, which is discussed in the next section. The average size of the core nanocrystal, d_c, estimated from the XRD profile via the Scherrer formula, was ∼8.5 nm (Supplementary Table 1 in ESI), which is in good agreement with the size obtained by TEM (8.5 ± 2.6 nm) (Figure 1 & Supplementary Figure 3A in ESI). Field emission–scanning electron microscopy images (Supplementary Figure 3B in ESI) show the morphology of Fe₃O₄, Fe₃O₄@PLA-PEG and Fe₃O₄@PLA-PEG/Cur samples. NPs can be seen as mostly spherical. The Fe₃O₄ MNPs functionalized by PLA-PEG and PLA-PEG/Cur are fairly uniform in size, with an average diameter, d_{NPs}, of about 10–12 nm, which is a few nanometers larger than the size of the bare Fe₃O₄ MNPs. The hydrodynamic sizes (d_h) of Fe₃O₄, Fe₃O₄@PLA-PEG and Fe₃O₄@PLA-PEG/Cur suspensions measured in water are shown in Supplementary Figure 4 (ESI). Fe₃O₄ NPs present an average hydrodynamic size of 37 nm, which is larger than the size obtained by TEM measurement. The average hydrodynamic size of Fe₃O₄@PLA-PEG
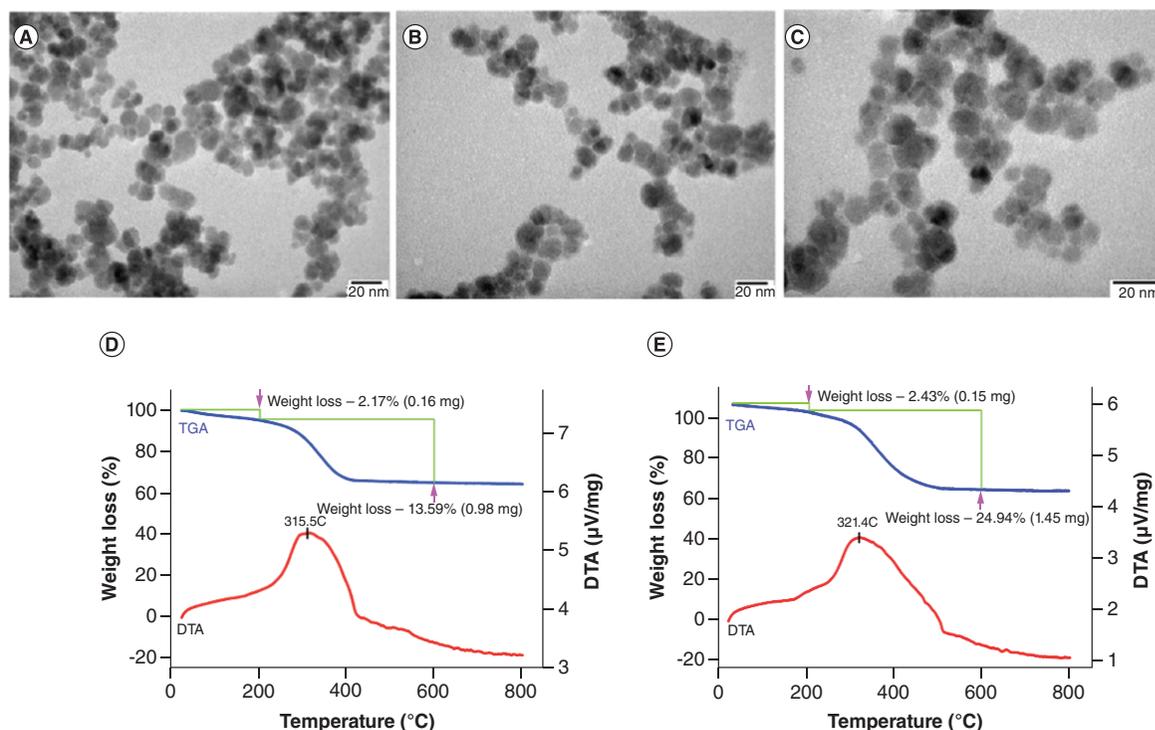
Figure 1.   Transmission electron microscopy images of Fe₃O₄ (A), Fe₃O₄@PLA-PEG (B) and Fe₃O₄@PLA-PEG/Cur (C) NPs (the scale bar in each image represents 20 nm) and thermogravimetric analysis (blue) and differential thermal analysis (red) diagrams of Fe₃O₄@PLA-PEG (D) and Fe₃O₄@PLA-PEG/Cur (E).
DTA: Differential thermal analysis; TGA: Thermogravimetric analysis.

rises to 45 nm, while this number of Fe₃O₄@PLA-PEG/Cur NPs is 52 nm. Dynamic light scattering data with narrow size distributions (Supplementary Figure 4 in ESI) and the zeta potential (Supplementary Table 1 in ESI) of the samples with values from -21.2 mV to -40.9 mV show that the samples were well dispersed and stable.

The Fe₃O₄@PLA-PEG and Fe₃O₄@PLA-PEG/Cur NPs were analyzed by TGA (Figure 1D & E) in order to estimate experimentally the mass contribution of nonmagnetic coating materials (i.e., PLA-PEG and curcumin) in the samples. The first weight-loss step in both diagrams around 100°C corresponds to the evaporation of water present in the samples. The next weight-loss step at above 300°C along with the exothermic peak in the differential thermal analysis curve is assigned to the decomposition of the organic components. The mass percentages of the organic components calculated from the initial mass of the precursors (i.e., Fe₃O₄, PLA-PEG and curcumin) of Fe₃O₄@PLA-PEG and Fe₃O₄@PLA-PEG/Cur were 9.1% and 25%, respectively. The values determined by TGA were 13.6 and 24.9%, which were quite compatible to the amount of the original ligands. The higher weight-loss percentage in Fe₃O₄@PLA-PEG/Cur compared with Fe₃O₄@PLA-PEG proves once again the presence of curcumin in Fe₃O₄@PLA-PEG/Cur. The curcumin content in Fe₃O₄@PLA-PEG/Cur NPs was then calculated to be ∼11%. The data also indicate that the mass percentages determined by TGA are in good agreement with those obtained from the initial composition.

Magnetization characteristics

Supplementary Figure 5A (ESI) presents the field dependent magnetisation (M-H) loops recorded at 300 K for the three samples – Fe₃O₄, Fe₃O₄@PLA-PEG and Fe₃O₄@PLA-PEG/Cur – measured for the total mass of the sample (i.e., core + shell). The influence of the shell coating and curcumin loading on the magnetic properties was studied based on changes in the magnetization (M) measured at 880 kA/m. For this, the magnetization of Fe₃O₄ cores (M_c) in Fe₃O₄@PLA-PEG and Fe₃O₄@PLA-PEG/Cur NPs was calculated considering the TGA percentage of Fe₃O₄ mass in the samples to be 74.7 and 70.4 Am²/kg, respectively. The slight decrease in M_c of Fe₃O₄@PLA-PEG/Cur NPs compared with that of Fe₃O₄@PLA-PEG NPs can result from the oxidation of the core in the process of curcumin loading onto the NPs.
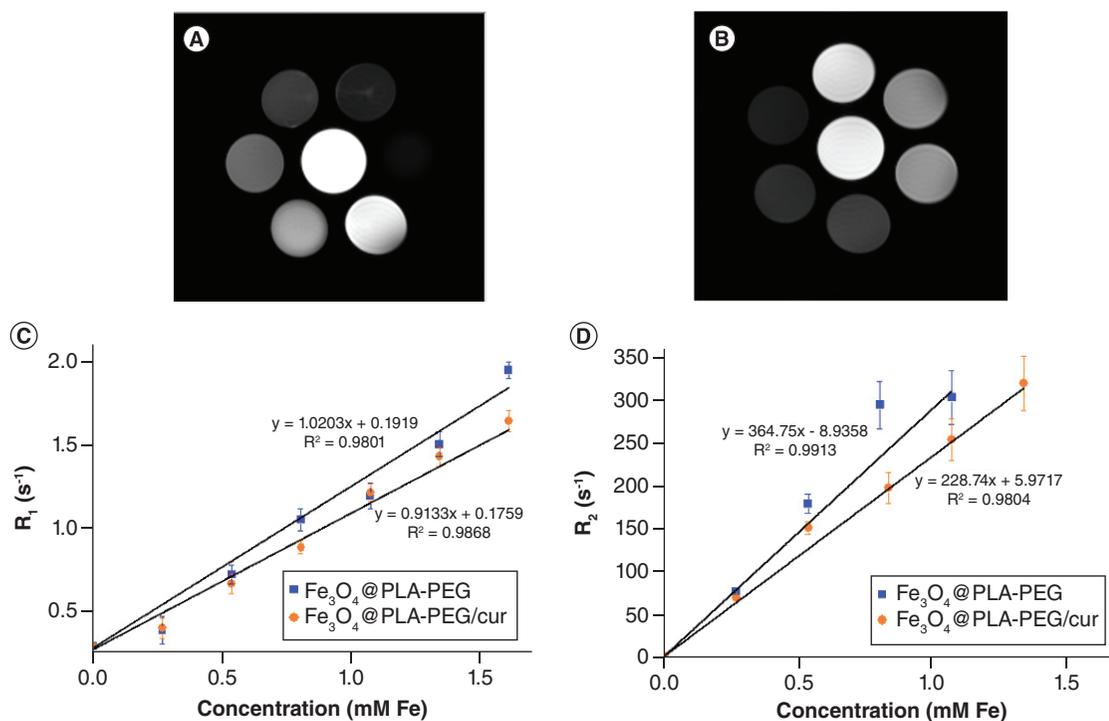
Figure 2.   T2-weighted MR images for (A) Fe$_3$O$_4$@PLA-PEG and (B) Fe$_3$O$_4$@PLA-PEG/curcumin suspensions and (C) R_1 and (D) R_2 relaxation rates for both samples as a function of the concentration of nanoparticles, together with their corresponding linear fittings.

The normalized M-H loops, using M_c, are presented in Supplementary Figure 5B (ESI). As clearly shown, the M_c value of the Fe$_3$O$_4$ core, after functionalization by PLA-PEG and loading curcumin, was ~10% larger compared to non coated one, which could be explained by the protection of the core from oxidation.

It is also worth noting in Supplementary Figure 5B that the hysteresis loops (i.e., M-H loops) present a very similar shape, with nearly zero coercivity and remanence, supposing a superparamagnetic behavior at room temperature. To confirm the superparamagnetic behavior of these samples, the M-H loops in Supplementary Figure 5B were fitted with a standard Langevin expression presented in Equation 4.

$$M(H) = M_S \int_0^\infty L\left(\frac{\mu H}{k_B T}\right) f(D)\, dD + \chi_{PM} H \qquad \text{(Equation 4)}$$

where D is the diameter of the NPs, $f(D)$ corresponds to a log-normal size distribution and $L(x) = \cot an(x) - 1/x$. The second term corresponds to a small paramagnetic contribution due to the atoms on the surface, χ_{PM} being the paramagnetic susceptibility. As can be seen in Supplementary Figure 5C (ESI), the fittings are really good, and the estimated average sizes are 9.1, 9.6 and 10.0 nm for Fe$_3$O$_4$, Fe$_3$O$_4$@PLA-PEG and Fe$_3$O$_4$@PLA-PEG/Cur samples, respectively. According to TEM and XRD, these values are close to the estimated core size, ~9 nm. The agreement confirms the superparamagnetic behavior of the MNPs.

High relaxivity r_2

MRI was performed with samples of varying concentrations of Fe$_3$O$_4$@PLA-PEG and Fe$_3$O$_4$@PLA-PEG/Cur nanocarriers. Figure 2A & B shows the spin echo images of Fe$_3$O$_4$@PLA-PEG and Fe$_3$O$_4$@PLA-PEG/Cur, respectively, while Figure 2C & D presents correspondingly the longitudinal and transverse relaxation rates, R_1 and R_2, of the two nanocarriers at various concentrations. The white central samples in Figure 2A & B were control samples of distilled water with no NPs. The following sequence images from white to black in clockwise order around the central samples correspond to the samples with concentrations 15, 30, 45, 60, 75 and 90 µg Fe/ml, respectively. There is a clear change in MRI contrast when increasing the sample concentration. Although the MR images became darker with increasing concentration in both samples, a higher MRI contrast enhancement was achieved for the Fe$_3$O$_4$@PLA-PEG sample. Similar results were also reported in some recent studies [47,63].

Sample	r_1 (mM s)$^{-1}$	r_2 (mM s)$^{-1}$	r_2/r_1	Core size (nm)	Ref.
Fe$_3$O$_4$@PLA-PEG (current study)	1.02	364.75	357.6	8.5	
Fe$_3$O$_4$@PLA-PEG/Cur (current study)	0.91	228.74	251.4	8.5	
Fe$_3$O$_4$-PEG-(NH$_2$)$_2$	22	191	24.8	12	[64]
Ferumoxytol	38	83	2.2	6.76	[65]
Fe$_3$O$_4$ PLA-TPGS†	0.3372	164.09	486.4	10	[33]
Fe$_3$O$_4$-dopamine-PEG and derivatives	-	79–110	-	5.5–7.4	[30]

Table 1. Relaxivity of the presently fabricated nanocarriers in comparison with some reference samples.

†TPGS is D-α-Tocopheryl polyethylene glycol 1000 succinate.
r_1 and r_2 are the longitudinal and transverse relaxivities, which were calculated using graphs 2C and 2D respective (see Equation 1).

To get quantitative information and to gain more insight into the effect of curcumin loading, ParaVision 5.1 software was used to calculate relaxation rate values from additional measurements of R_1 and R_2 for the Fe$_3$O$_4$@PLA-PEG and Fe$_3$O$_4$@PLA-PEG/Cur specimens in the concentration range 0–1.6 mM of Fe. As seen in the graphs (Figure 2C & D), linear dependencies are observed in general fitted lines with a high correlation factor (R^2 ≥0.98) in the whole range of measured concentrations – that is, up to 1.6 mM (90 μg/ml Fe) for the longitudinal relaxation and up to 1.0 mM (56 μg/ml Fe) for the transverse relaxation. It can be observed that the relaxation rate for the Fe$_3$O$_4$@PLA-PEG/Cur sample keeps a good linear relationship with concentration for both longitudinal and transverse regimes in the whole dilution range. For the Fe$_3$O$_4$@PLA-PEG sample, however, there is an evident change in the evolution of the R_2 relaxation rate with increasing concentration, and the linear behavior is apparently lost after 1 mM. This observation suggests that the presence of curcumin in the core of Fe$_3$O$_4$@PLA-PEG/Cur may help reduce the attraction between the MNPs and make the curcumin-loaded conjugates better dispersed than the nonloaded ones at high concentrations, which is important for the final biomedical application.

The obtained relaxivity values, r_1 and r_2 (calculated in the linear concentration region), are collected in Table 1.

MFH studies

The heating efficiency of Fe$_3$O$_4$@PLA-PEG and Fe$_3$O$_4$@PLA-PEG/Cur NPs after dispersion in water at a concentration of 1.63 mg$_{Fe}$/ml was studied using calorimetric methods. The temperature versus time curves were recorded for different AMF (Supplementary Figure 6 in ESI). As depicted, the heating rate rapidly increases with increasing field, and the therapeutic window for hyperthermia therapy, 40–45°C, can be easily reached within around 10 min by modifying the amplitude of the AMF during the treatment. To get a better insight into the hyperthermic effect of the MNPs, the authors calculated the heating efficiency or SAR (Supplementary Table 2 in ESI). The obtained SAR values were calculated for the Fe$_3$O$_4$@PLA-PEG/Cur samples measured at a frequency of 178 kHz and Fe concentration of 1.63 mg.ml^{-1}. The obtained SAR values follow an H^2 dependence (Supplementary Figure 7 in ESI), as expected according to the linear response theory [66]. Although the H×f values for the experiments were slightly higher than the Atkinson–Brezovich limit [54], many other studies also used fields with higher H×f values [67–69]. The calculation of the intrinsic loss power (ILP), SAR/(f×H^2), gave a value of 11.5 nHm^{2}kg^{-1} (H = 3600 A/m; f = 178 kHz) for Fe$_3$O$_4$@PLA-PEG/Cur sample, which is appreciably greater than those commercial iron oxide-based NPs reported in the literature (e.g., Resovist presents an ILP of 1.5 nHm^{2}kg^{-1} [61]). The PLA-PEG and Cur might contribute to improvement of the SAR and ILP value of the NPs. A recent study has reported that SAR and ILP were influenced by size and the structure of iron oxide nanoflowers, which depended on the polyacrylic acid concentration during the synthesis [70].

Effective release by remote AMF-mediated control

The first experimental series for curcumin release efficiency was performed in five samples after applying the same AMF field of 5040 A/m for 5, 10, 15, 20 and 25 min. The release percentages of all analyzed samples are depicted in Figure 3. It is clear that longer exposure time, simultaneously with the higher temperature reached in the solution, resulted in a higher curcumin release. After 20 min under the applied AMF, the curcumin amount loaded in the Fe$_3$O$_4$@PLA-PEG/Cur was almost fully released and reached plateau.

On the other hand, the passive curcumin release in an incubated bath at 37°C, as shown in Figure 3, reached a saturation release level of about 80%, only after 24 h. Isothermal AMF release rates for the Fe$_3$O$_4$@PLA-PEG/Cur
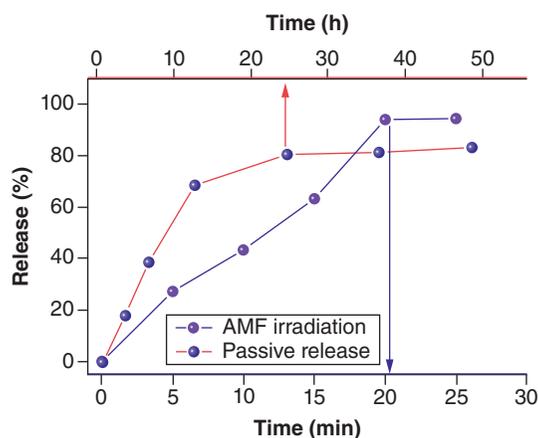
Figure 3. Cumulative curcumin release versus alternating magnetic field irradiation time and passive release at 37°C. AMF: Alternating magnetic field.

Table 2. Release experiments by irradiation of alternating magnetic field at different temperatures.			
Temperature reached by AMF (°C)	Field strength (A/m)	Time required to reach targeted temperature (s)	Curcumin release (%)
37	3600	897	40.2
	3760	742	37.5
	4000	479	36.1
	4240	363	34.2
45	4000	1024	60.2
	4240	716	55.4
	4400	605	52.3
	5040	412	50.1

ferrofluid were estimated by varying the field and time for the solution to reach 37°C and 45°C. The experimental conditions are described in Table 2.

The UV-VIS spectra and calculated curcumin released amounts are depicted in Supplementary Figure 8 (ESI). As shown in Table 2, the stronger the magnetic field, the shorter the time required to reach the temperature, and the curcumin released amount depends on both the temperature and the duration to reach to that temperature. This allows the drug release to be controlled by adjusting the magnetic field strength and/or AMF exposure time.

From the inductive heating curve in Supplementary Figure 9 (ESI) & Table 2, the authors could estimate the initial release rate as equal to 40%/h and 51%/h at T = 37°C and 45°C, respectively, which are in agreement with the values of 18%/h and 26%/h observed by Purushotham and Ramanujan [40]. The application of AMF made the release faster and more efficient compared to passive release. The faster rate accompanied by higher percentage release that was observed for the Fe$_3$O$_4$@PLA-PEG/Cur nanocarrier as compared with other reports [40,71] might originate from different functionalizing materials and/or drug molecules, namely thermosensitive polymer and doxorubicin [40], PLA and pluronic F127 [72] and alginate [71].

In vivo MRI experiments

MR images were taken for control mouse A and tumor-bearing mice B, C and D. For mice C and D, 10 and 50 μl of Fe$_3$O$_4$@PLA-PEG magnetic fluid were directly injected into their tumors. Figure 4A shows the images of the tumor region in the mice right after injection. It seems that no organs or tumors could be identified in these images. As shown in Figure 4B, for mice C and D, there was a distinct dark area, different from the control mouse. The tumors in mice B, C and D can be identified, and a better contrast in the tumor area and the tumor's rim can be seen as well as the size of the tumor (the red arrow) for mice C and D, injected with Fe$_3$O$_4$@PLA-PEG magnetic fluid.

Figure 5A presents the obtained MR images for mice C and D at different time periods after injection. As depicted, all tumor positions could be clearly seen at all times and MNPs were observed dispersing in the tumor over time. From 30 to 45 min after injection, the MNPs were evenly distributed and gave the highest contrast for MRI. For observation of smaller tumors, 5-day-old tumors were scanned with an MRI e-scanner in a similar
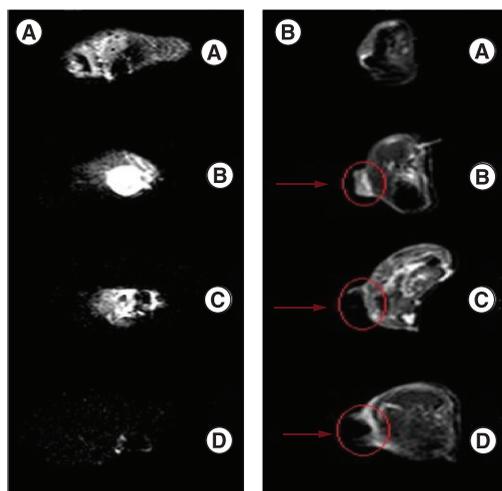
Figure 4.   MRI images of transverse (panel A) and longitudinal (panel B) MRI scans right after injection (0 min) of normal mouse as biological control (mouse A), noninjected mouse with tumor as cancer control (mouse B), injected 10 μl magnetic fluid (mouse C) and injected 50 μl magnetic fluid (mouse D).
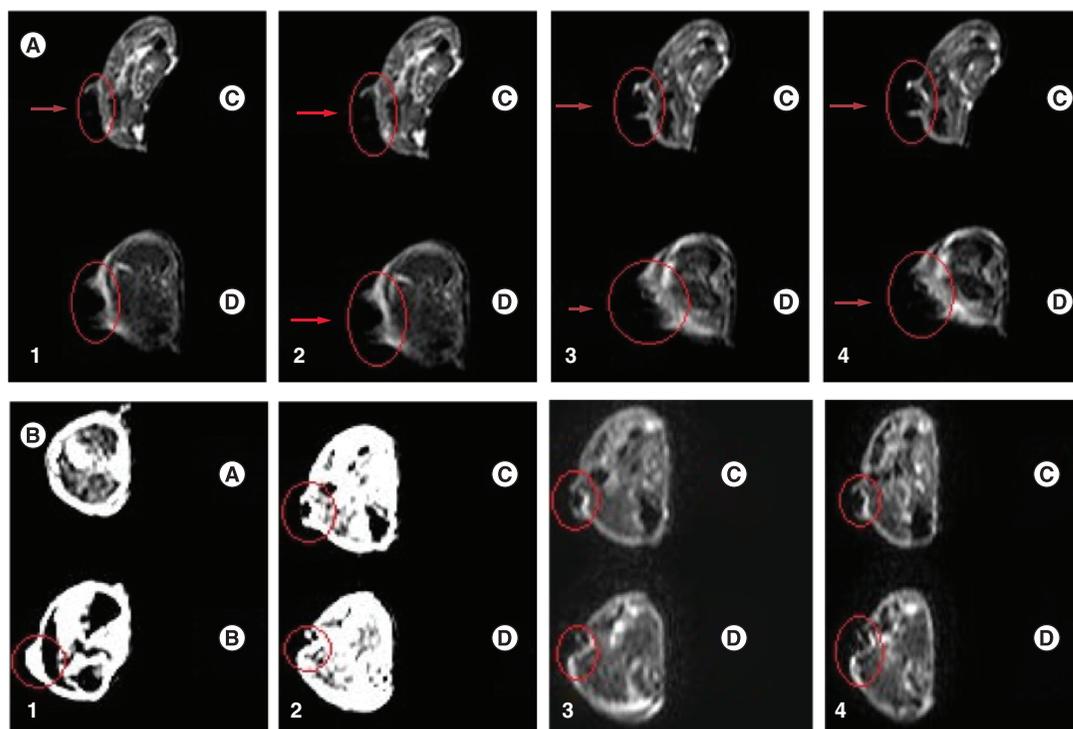

Figure 5.   MRI images of (panel A) adult tumors on mouse C and mouse D after (1) 0 min, (2) 15 min, (3) 30 min and (4) 45 min (red circles mark the tumor positions) and (panel B) 5-day-old tumors on (1) mouse A (biological control), mouse B (cancer control); mouse C (injected 10 μl magnetic fluid) and mouse D (injected 50 μl magnetic fluid) after (2) 0 min, (3) 15 min and (4) 30 min.

procedure compared with the adult tumors. Figure 5B shows that, with mice C and D, there was a marked dark area, different from the cancer control mouse – mouse B. The contrast in the tumor area and the tumor's rim as well as the size of the tumor (the red circle) were easily observed in mice C and D.

Treatment of the tumor by MFH with Fe_3O_4@PLA-PEG

Figure 6 shows the tumor image and size variations during the treatment for the experimental mice, 5 and 10 days after tumor implantation. For the treated mice with 5-day-old cancer, the tumor volume decreased strongly, so that 50% of them exhibited almost a disappearance of the tumor after three MFH treatments. The effect could be seen right after the first MFH treatment when the tumor surface clearly shrank with the appearance
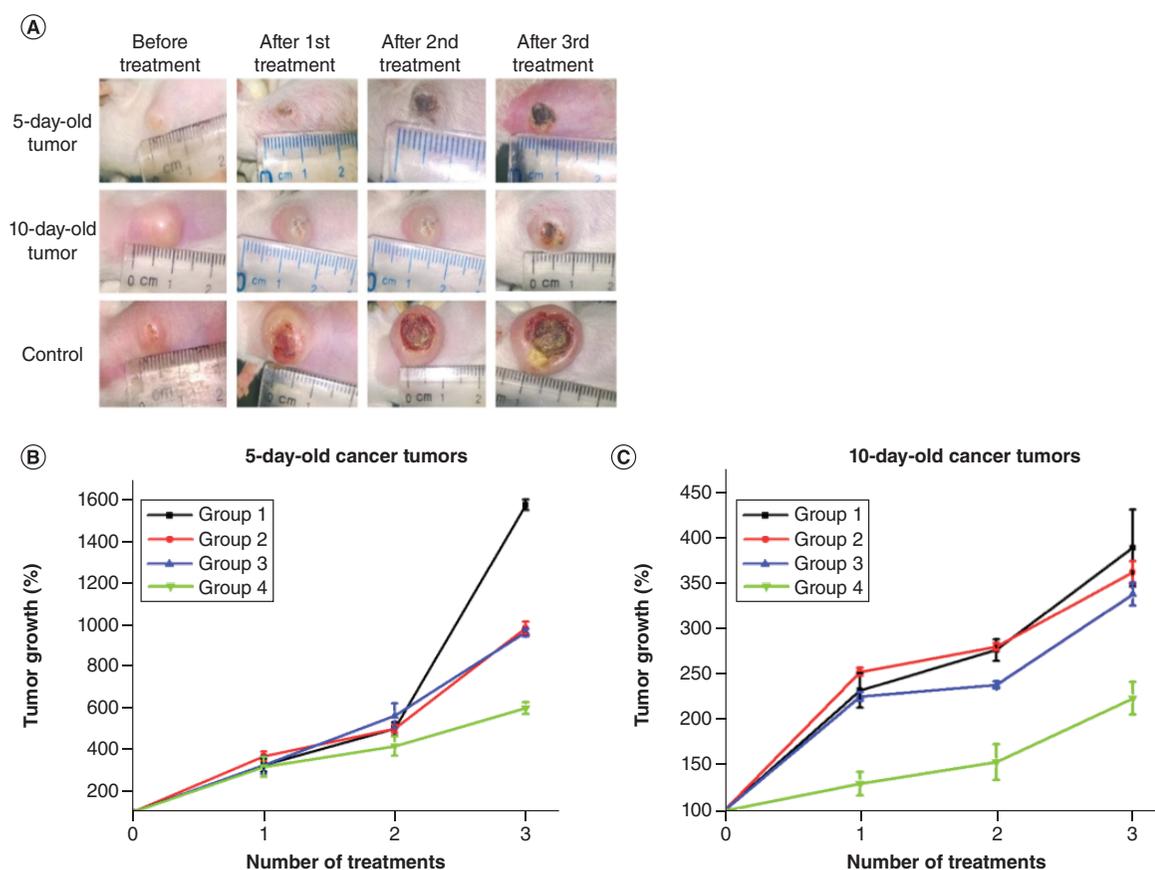
Figure 6. Changes in tumor growth during the magnetic fluid hyperthermia therapy of mice at day 5 and day 10 after cancer incubation. (A) By images and size changes by graph for the tumor (B) at day 5 and (C) at day 10. Group 1: noninjected and nonirradiated mice as a control; group 2: noninjected mice with alternating magnetic field (AMF) irradiation; group 3: mice injected with Fe₃O₄ @PLA-PEG and without AMF irradiation; group 4: mice injected with Fe₃O₄ @PLA-PEG and subjected to AMF.

of black eschar covering the wound. After treatment time, the eschar fell off by itself and left a scar behind where fur could grow back normally. For the treated mice with 10-day-old cancer, although the tumor did not disappear totally after treatment, its development was seriously inhibited. The growth after 3 treatments of 5-day-old tumor was 600%, which is equivalent to 37–38% compared with the tumor growth in the control group (1600%; Figure 6B). For the 10-day-old tumor, the treatment effectiveness was lower but still clearly evident as compared with untreated mice (Figure 6).

Observation of regrowth of the tumor after the treatment was performed starting at day 1 after the last MFH therapy. The graphs obtained for the two categories of cancer mice are presented in Supplementary Figure 10 (ESI). For the mice with cancer that was 5-day-old, the tumor continued to decrease for 4–5 days after the last MFH treatment and remained unchanged for the following 2 days after that. Eight days after the treatment, the tumor seemed to develop but at such a slow rate that at day 14 the tumor was almost of the size observed just after the treatment (Supplementary Figure 10A, ESI). For the mice with 10-day-old cancer, Supplementary Figure 10B (ESI) depicts that 4–5 days after the last MFH therapy, the tumor volume slightly decreased, and it started to grow again after the day 5 post-treatment, so that on day 14 it reached 150% growth rate as compared with the size after the last treatment.

Discussion

PLA-PEG is an amphiphilic copolymer in which PEG hydrophilic chains tend to extend outside, while PLA hydrophobic chains arrange inside the micelles. The NPs could be encapsulated via the PEG segment [73] and curcumin is loaded into the NP carrier (Supplementary Figure 1 in ESI). For Fe₃O₄@PLA-PEG/Cur NPs,

curcumin molecules might penetrate into the copolymer micelles' center with PLA hydrophobic segments (as observed in the authors' previous Cur/PLA-PEG nanosystems [74] and other reports [58,75,76]). The increase in the hydrodynamic size of the Fe_3O_4 MNPs compared with their size obtained by TEM can be explained by the adsorption of OH^- ions and H_2O molecules through hydrogen bonding in the aqueous solution onto the surface of the Fe_3O_4 MNPs. The hydrodynamic size of Fe_3O_4@PLA-PEG rises due to the water expansion of the hydrophilic PEG component in the outermost shell of the particles. A similar observation has been reported [77,78]. The curcumin present in the core of Fe_3O_4@PLA-PEG/Cur may lead to an increase in the size of the core, and therefore the overall size of NPs when in water (Supplementary Table 1 in ESI).

The ~10% increase in the net magnetization of the NPs after coating and drug loading shows an important role of surface functionalization of NPs. A similar increase in the net magnetization of the NPs has been reported in the literature for different kinds of coatings [79–81] and attributed to an enhancement of the surface magnetic ordering of the MNPs due to the coating [29]. In addition, the obtained M_c^{TGA} values become closer to the saturation magnetization of bulk Fe_3O_4 (~92 Am^2/kg), which, as explained before, is especially important for biomedical applications. High magnetization could result in good MRI and MFH effects.

In the *in vitro* MRI experiments, the $r_{1,2}$ values of the Fe_3O_4@PLA-PEG/Cur samples being smaller than those of Fe_3O_4@PLA-PEG can be explained by the reduction in magnetization upon curcumin encapsulation from 74.7 and 70.4 Am^2/kg (Supplementary Figure S5 in ESI), which in turn decrease the transverse relaxivity of the MNPs [3]. It is worth noting that the change in the r_2/r_1 ratio for the case of Fe_3O_4@PLA-PEG/Cur (Table 1) can be related to the effect of curcumin adsorption on the Fe_3O_4 NP surface, which resulted in a hydrophobicity change of the whole coating layer [82].

Notably, r_2 values of both Fe_3O_4@PLA-PEG and Fe_3O_4@PLA-PEG/Cur samples are significantly higher than those obtained for commercial Resovist, ferumoxytol or other Fe_3O_4-based systems [8,30,33,83]. The high value of the r_2/r_1 ratio also indicates that the T_2 contrast mechanism is dominant for the investigated nanocarriers. The *in vivo* MRI results reconfirm that the MNPs enhance the contrast in MRI observation. The authors performed the *in vivo* MRI experiment in the 5-day-old tumor to determine if the MNPs could help distinguish the tumor from its surroundings at its early stage. From Figure 5B, one can note that the MNPs allow a more accurate assessment of the size, shape and part of the internal structure of the tumor at the early stage of cancer as well as an easier assessment of the presence or absence of a tumor when it appears inside the body. The MRI study on a 5-day-old tumor can also illustrate the MRI contrast enhancement for tumor observation, even at its early stage. In Figure 5A & B, a 10 µl dose of the NPs shows better differentiation of the rim and the inside area of the tumor than a 50 µl dose does. Therefore, a 10 µl dose (1.8 mg Fe/kg body weight) is better for MRI contrast enhancement. Some other studies used higher doses for MRI *in vivo* experiments (5 mg/kg [36,84]), and Chen *et al.* used an even higher dose of 30 mg/kg [85].

As indicated from the heating curves measured at f = 178 kHz and H_{AC} = 5040 A/m (Supplementary Figure 8 in ESI), the Fe_3O_4@PLA-PEG and Fe_3O_4@PLA-PEG/Cur ferrofluids reached the temperature range for cancer hyperthermia treatment after a few hundredths of seconds. That makes them both potential candidates for low-field hyperthermia therapy, combined with heat-activated drug-release chemotherapy. The AMF-mediated drug-release profile clearly indicates that the heat generation of the MNPs activated by AMF serves as a driving force to release curcumin from the hydrophobic core of the system in a much faster and more effective way as compared with passive release. Although this phenomenon has also been reported by other researchers, most of the research involved thermosensitive components in the NPs [40,86–88]. The low passive rate achieves nearly zero losses of curcumin at the beginning, and then high active rate release, within a few minutes, allows a remotely controlled targeted delivering.

The biodistribution of NPs depends on many factors such as chemical composition, size, shape and surface modifications [89]. In a previous report, by *ex vivo* MFH experiments and atomic absorption spectroscopy analysis, the authors of the current study found that when intravenously injected into mice, the amounts of Fe_3O_4@PLA-PEG MNPs are distributed in organs in the following order: liver > lung > spleen > tumor > kidney [90]. More important, a dose that is sufficient for hyperthermia of the tumor would overheat the liver. Therefore, in this study, to evaluate the cancer treatment ability of Fe_3O_4@PLA-PEG MNPs by MFH, the MNPs were directly injected into the mice's tumors. The product H×f of the magnetic field used in these *in vivo* experiments (8.97 × 10^8 A/(ms)), although slightly higher than that in the Atkinson–Brezovich criteria (5 × 10^8) [10], is lower than that in the Dutz–Hergt criteria (5 × 10^9) [55] is also much lower than that of many published Fe_3O_4-based NPs [56]. Compared with 19 nm cubic Fe_3O_4 NPs at the higher H×f = 1.21 × 10^9 A/[ms], Fe_3O_4@PLA-PEG MNPs show a similar effect of tumor growth inhibition [86].

The observed efficiency of MFH therapy is also in agreement with several other reports on similar treatments such as via direct injection of MNPs into breast tumors [91] or brain tumors [92].

Conclusion

We have developed a multifunctional magnetic nanosystem with a core-shell structure consisting of ∼9 nm Fe$_3$O$_4$ MNPs surrounded by amphiphilic copolymer PLA-PEG coating (Fe$_3$O$_4$@PLA-PEG) that allows us to reduce the coating mass. Besides, the coating layer helps improve the magnetic properties of the nanosystem by increasing the saturation magnetization of the NPs (∼10%). The high relaxivity ratio (r_2/r_1 = 357.6) indicates that Fe$_3$O$_4$@PLA-PEG MNPs can effectively work as T_2 contrast agents for MRI. In addition, the high heating efficiency obtained under AMF (SAR = 82.2 W/g at H = 5–40 A/m; f = 178 kHz) reveals that Fe$_3$O$_4$@PLA-PEG MNPs are also very promising for magnetic hyperthermia. In addition, these nanocarriers can be loaded with anticancer drug curcumin (Fe$_3$O$_4$@PLA-PEG/Cur) and release the drug under the application of an external AMF in a fast, facile and efficient way (nearly 100% release after 20 min). *In vivo* studies with mice bearing sarcoma 180 cancer reveal that the mice injected with Fe$_3$O$_4$@PLA-PEG and treated with AMF showed clear tumor growth inhibition lasting several days after the hyperthermia treatment. Finally, *in vivo* MRI experiments clearly showed an improvement in the contrast in the tumor area for those mice injected with Fe$_3$O$_4$@PLA-PEG MNPs. Therefore, our study indicates that Fe$_3$O$_4$@PLA-PEG/Cur is a promising multifunctional nanosystem, providing both efficient cancer detection (MRI) and treatment (drug delivery and magnetic hyperthermia) capacities.

Future perspective

The combination effect of chemotherapy using curcumin or other cancer drugs with magnetic hyperthermia should be conducted. The heat dose, the heat map of magnetic hyperthermia are vital for the translation of this modality of treatment to clinics and hence will be studied.

Summary points

- A novel drug nanocarrier of Fe$_3$O$_4$@PLA-PEG was designed and fabricated for multipurpose applications.
- The 8.5 nm Fe$_3$O$_4$ core was covered with the polymeric matrix of polylactic acid (PLA)-PEG to encapsulate an anticancer agent of curcumin at a content of ∼11%.
- Calculated magnetizations for the magnetic component (Fe$_3$O$_4$ core) of Fe$_3$O$_4$@PLA-PEG and Fe$_3$O$_4$@PLA-PEG/Cur were 74.7 and 70.4 Am^2/kg, respectively.
- A high specific absorption rate value of 82.2 W/g was achieved at a low field and frequency of H = 5040 A/m, f = 178 kHz.
- Curcumin could be controllably released by an alternating magnetic field from the magnetic carriers.
- The nanosystems significantly increased the transverse relaxivity value (r_2 = 364.75 mM^{-1} s^{-1}).
- The tumor could be observed by MRI with the enhancement contrast by the magnetic carriers.
- Magnetic fluid hyperthermia could effectively reduce the tumor size in mice bearing sarcoma 180 *in vivo*.

Ethical conduct of research

The authors state that all experiments involving animals were performed according to strict NIH guidelines for the care and use of laboratory animals (NIH Publication No. 85-23 Rev. 1985) and was approved by the Dinh Tien Hoang Institute of Medicine, Hanoi, Vietnam.

References

Papers of special note have been highlighted as: ● of interest

1. Bruchez M, Moronne M, Gin P, Weiss S, Alivisatos AP. Semiconductor nanocrystals as fluorescent biological labels. *Science (80-.)* 281(5385), 2013–2016 (1998).

2. Ferrari M. Cancer nanotechnology: opportunities and challenges. *Nat. Rev. Cancer* 5(3), 161–171 (2005).

3. Hilger I, Kaiser WA. Iron oxide-based nanostructures for MRI and magnetic hyperthermia. *Nanomedicine* 7(9), 1443–1459 (2012).

4. Dave SR, Gao X. Monodisperse magnetic nanoparticles for biodetection, imaging, and drug delivery: a versatile and evolving technology. *Wiley Interdiscip. Rev. Nanomed. Nanobiotechnol.* 1(6), 583–609 (2009).

5. *Clinical Applications of Magnetic Nanoparticle from Fabrication to Clinical Applications.* Nguyen TKT (Ed.). CRC Press, Taylor & Francis, NY, USA (2017).

6. Pankhurst QA, Thanh NTK, Jones SK, Dobson J. Progress in applications of magnetic nanoparticles in biomedicine. *J. Phys. D. Appl. Phys.* 42(22), 224001 (2009).

7. *Magnetic Nanoparticles: From Fabrication to Clinical Applications.* Nguyen TKT (Ed.). CRC Press, Taylor & Francis, NY, USA (2012).

8. Corot C, Robert P, Idée JM, Port M. Recent advances in iron oxide nanocrystal technology for medical imaging. *Adv. Drug Deliv. Rev.* 58(14), 1471–1504 (2006).

9. Gupta A, Gupta M. Synthesis and surface engineering of iron oxide nanoparticles for biomedical applications. *Biomaterials* 26(18), 3995–4021 (2005).

10. Laurent S, Forge D, Port M *et al.* Magnetic iron oxide nanoparticles: synthesis, stabilization, vectorization, physicochemical characterizations, and biological applications (vol 108, pg 2064, 2008). *Chem. Rev.* 110(4), 2574 (2010).

● **Although this review was published in 2010, the systematic information provided is relevant for current studies.**

11. Grasset F, Duguet E, Mornet S, Vasseur S. Magnetic nanoparticle design for medical diagnosis and therapy. *J. Mater. Chem.* 14(14), 2161–2175 (2004).

12. Pankhurst QA, Connolly J, Jones SK, Dobson J. Applications of magnetic nanoparticles in biomedicine. *J. Phys. D. Appl. Phys.* 36(13), R167 (2003).

13. Pantic I. Magnetic nanoparticles in cancer diagnosis and treatment: novel approaches. *Synthesis (Stuttg.)* 26, 67–73 (2010).

14. Reddy LH, Arias JL, Nicolas J, Couvreur P. Magnetic nanoparticles: design and characerization, toxicity and biocompatibility, pharmaceutical and biomedical applications. *Chem. Rev.* 112, 5818–5878 (2012).

15. Wilhelm C, Gazeau F, Bacri J-C. Magnetophoresis and ferromagnetic resonance of magnetically labeled cells. *Eur. Biophys. J.* 31(2), 118–125 (2002).

16. Bin NH, Song IC, Hyeon T. Inorganic nanoparticles for MRI contrast agents. *Adv. Mater.* 21(21), 2133–2148 (2009).

17. Lacroix L-M, Ho D, Sun S. Magnetic nanoparticles as both imaging probes and therapeutic agents. *Curr. Top. Med. Chem.* 10(12), 1184–1197 (2010).

18. Matsumoto Y, Jasanoff A. T2 relaxation induced by clusters of superparamagnetic nanoparticles: Monte Carlo simulations. *Magn. Reson. Imaging* 26(7), 994–998 (2008).

19. Sosnovik DE, Nahrendorf M, Weissleder R. Magnetic nanoparticles for MR imaging: agents, techniques and cardiovascular applications. *Basic Res. Cardiol.* 103(2), 122–130 (2008).

20. Wang Y, Hussain S, Krestin G. Superparamagnetic iron oxide contrast agents: physicochemical characteristics and applications in MR imaging. *Eur. Radiol.* 11(11), 2319–2331 (2001).

21. Mukesh GH, Jelle B, Peter FH *et al.* Noninvasive detection of clinically occult lymph-node metastases in prostate cancer. *N. Engl. J. Med.* 34825, 2491–2499 (2003).

22. Jordan A, Scholz R, Wust P, Fähling H, Felix R. Magnetic fluid hyperthermia (MFH): cancer treatment with AC magnetic field induced excitation of biocompatible superparamagnetic nanoparticles. *J. Magn. Magn. Mater.* 201(1), 413–419 (1999).

23. Imashiro C, Takeshita H, Morikura T, Miyata S, Takemura K, Komotori J. Development of accurate temperature regulation culture system with metallic culture vessel demonstrates different thermal cytotoxicity in cancer and normal cells. *Sci. Rep.* 11(1), (2021).

- This article provides a novel apparatus to more accurately evaluate the culture medium in a thermal cytotoxicity study.

24. Hedayatnasab Z, Abnisa F, Daud WMAW. Review on magnetic nanoparticles for magnetic nanofluid hyperthermia application. *Mater. Des.* 123, 174–196 (2017).

25. Beik J, Abed Z, Ghoreishi FS *et al.* Nanotechnology in hyperthermia cancer therapy: from fundamental principles to advanced applications. *J. Control. Rel.* 235, 205–221 (2016).

26. Lavorato GC, Das R, Alonso Masa J, Phan MH, Srikanth H. Hybrid magnetic nanoparticles as efficient nanoheaters in biomedical applications. *Nanoscale Adv.* 3(4), 867–888 (2021).

- This article provides information on multiple inorganic materials in magnetic nanoparticles for efficient heat delivery.

27. Mohammed L, Gomaa HG, Ragab D, Zhu J. Magnetic nanoparticles for environmental and biomedical applications: a review. *Particuology* 30, 1–14 (2017).

28. Daou TJ, Grenèche JM, Pourroy G *et al.* Coupling agent effect on magnetic properties of functionalized magnetite-based nanoparticles. *Chem. Mater.* 20(18), 5869–5875 (2008).

29. Nagesha DK, Plouffe BD, Phan M, Lewis LH, Sridhar S, Murthy SK. Functionalization-induced improvement in magnetic properties of Fe₃O₄ nanoparticles for biomedical applications. *J. Appl. Phys.* 105(7), 2–4 (2009).

30. Smolensky ED, Park HYE, Berquó TS, Pierre VC. Surface functionalization of magnetic iron oxide nanoparticles for MRI applications – effect of anchoring group and ligand exchange protocol. *Contrast Media Mol. Imaging* 6(4), 189–199 (2011).

31. Truong Phuoc L, Jouhannaud J, Pourroy G. Magnetic iron oxide and the effect of grafting on the magnetic properties. Presented at: *Proceedings of SPIE.* Incheon, Republic of Korea (24 October 2012).

32. Hickey RJ, Haynes AS, Kikkawa JM, Park S-J. Controlling the self-assembly structure of magnetic nanoparticles and amphiphilic block-copolymers: from micelles to vesicles. *J. Am. Chem. Soc.* 133(5), 1517–1525 (2011).

33. Prashant C, Dipak M, Yang CT, Chuang KH, Jun D, Feng SS. Superparamagnetic iron oxide – loaded poly (lactic acid)-d-α-tocopherol polyethylene glycol 1000 succinate copolymer nanoparticles as MRI contrast agent. *Biomaterials* 31(21), 5588–5597 (2010).

34. Lodge TP, Pudil B, Hanley KJ. The full phase behavior for block copolymers in solvents of varying selectivity. *Macromolecules* 35(12), 4707–4717 (2002).

35. Torchilin VP. PEG-based micelles as carriers of contrast agents for different imaging modalities. *Adv. Drug Deliv. Rev.* 54(2), 235–252 (2002).

36. Wang Y, Ng YW, Chen Y *et al.* Formulation of superparamagnetic iron oxides by nanoparticles of biodegradable polymers for magnetic resonance imaging. *Adv. Funct. Mater.* 18(2), 308–318 (2008).

37. Yallapu MM, Nagesh PKB, Jaggi M, Chauhan SC. Therapeutic applications of curcumin nanoformulations. *AAPS J.* 17(6), 1341–1356 (2015).

38. Yallapu MM, Jaggi M, Chauhan SC. Curcumin nanoformulations: a future nanomedicine for cancer. *Drug Discov. Today* 17(1–2), 71–80 (2012).

39. Thu HP, Quang DT, Trang MTT *et al. In vitro* apoptosis enhancement of Hep-G2 cells by PLA-TPGS and PLA-PEG block copolymer encapsulated curcumin nanoparticles. *Chem. Lett.* 42(3), 255–257 (2013).

40. Purushotham S, Ramanujan RV. Thermoresponsive magnetic composite nanomaterials for multimodal cancer therapy. *Acta Biomater.* 6(2), 502–510 (2010).

41. Hayashi K, Ono K, Suzuki H *et al.* High-frequency, magnetic-field-responsive drug release from magnetic nanoparticle/organic hybrid based on hyperthermic effect. *ACS Appl. Mater. Interfaces* 2(7), 1903–1911 (2010).

42. Ha PT, Le TTH, Bui TQ, Pham HN, Ho AS, Nguyen LT. Doxorubicin release by magnetic inductive heating and *in vivo* hyperthermia-chemotherapy combined cancer treatment of multifunctional magnetic nanoparticles. *New J. Chem.* 43, 5404–5413 (2019).

43. Nasery MM, Abadi B, Poormoghadam D. Curcumin delivery mediated by bio-based nanoparticles: a review. *Molecules* 25(1-28), 1689 (2020).

44. Yao Y, Zhao D, Li N *et al.* Multifunctional Fe₃O₄@Polydopamine@DNA-fueled molecular machine for magnetically targeted intracellular Zn²⁺ imaging and fluorescence/MRI guided photodynamic-photothermal therapy. *Anal. Chem.* 91(12), 7850–7857 (2019).

45. Hadjipanayis CG, Bonder MJ, Balakrishnan S, Wang X, Mao H, Hadjipanayis GC. Metallic iron nanoparticles for MRI contrast enhancement and local hyperthermia. *Small* 4(11), 1925–1929 (2008).

46. Guardia P, Batlle-Brugal B, Roca AG *et al.* Surfactant effects in magnetite nanoparticles of controlled size. *J. Magn. Magn. Mater.* 316(2 SPEC. ISS.), 756–759 (2007).

47. Arsalani S, Guidelli EJ, Silveira MA *et al.* Magnetic Fe$_3$O$_4$ nanoparticles coated by natural rubber latex as MRI contrast agent. *J. Magn. Magn. Mater.* 475, 458–464 (2019).

48. Kozenkova E, Levada K, Efremova MV *et al.* Multifunctional Fe$_3$O$_4$-au nanoparticles for the MRI diagnosis and potential treatment of liver cancer. *Nanomaterials* 10(9), 1–15 (2020).

49. Sanson C, Diou O, Thévenot J *et al.* Doxorubicin loaded magnetic polymersomes: theranostic nanocarriers for MR imaging and magneto-chemotherapy. *ACS Nano* 5(2), 1122–1140 (2011).

50. Phong PT, Nguyen LH, Manh DH, Lee I-J, Phuc NX. Computer simulations of contributions of Néel and Brown relaxation to specific loss power of magnetic fluids in hyperthermia. *J. Electron. Mater.* 46(4), 2393–2405 (2017).

51. Khurshid H, Alonso J, Nemati Z *et al.* Anisotropy effects in magnetic hyperthermia: a comparison between spherical and cubic exchange-coupled FeO/Fe$_3$O$_4$ nanoparticles. *J. Appl. Phys.* 117(17) (2015).

52. Nemati Z, Das R, Alonso J, Clements E, Phan MH, Srikanth H. Iron oxide nanospheres and nanocubes for magnetic hyperthermia therapy: a comparative study. *J. Electron. Mater.* 46(6), 3764–3769 (2017).

53. Nemati Z, Alonso J, Martinez LM *et al.* Enhanced magnetic hyperthermia in iron oxide nano-octopods: size and anisotropy effects. *J. Phys. Chem. C* 120(15), 8370–8379 (2016).

54. Atkinson WJ, Brezovich IA, Chakraborty DP. Usable frequencies in hyperthermia with thermal seeds. *IEEE Trans. Biomed. Eng.* BME-31(1), 70–75 (1984).

55. Dutz S, Hergt R. Magnetic nanoparticle heating and heat transfer on a microscale: basic principles, realities and physical limitations of hyperthermia for tumour therapy. *Int. J. Hyperth.* 29(8), 790–800 (2013).

56. Rodrigues HF, Capistrano G, Bakuzis AF. *In vivo* magnetic nanoparticle hyperthermia: a review on preclinical studies, low-field nano-heaters, noninvasive thermometry and computer simulations for treatment planning. *Int. J. Hyperth.* 37(3), 76–99 (2020).

•   **Low-field application of magnetic nanoparticles is discussed.**

57. Varaprasad K, Yallapu MM, Núñez D *et al.* Generation of engineered core-shell antibiotic nanoparticles. *RSC Adv.* 9(15), 8326–8332 (2019).

58. Thong PQ, Nam NH, Phuc NX, Manh DH, Thu HP. Impact of PLA/PEG ratios on curcumin solubility and encapsulation efficiency, size and release behavior of curcumin loaded poly(lactide)-poly(ethyleneglycol) polymeric micelles. *Int. J. Drug Deliv.* 6(3), 279–285 (2014).

59. Thu Huong LT, Nam NH, Doan DH *et al.* Folate attached, curcumin loaded Fe$_3$O$_4$ nanoparticles: a novel multifunctional drug delivery system for cancer treatment. *Mater. Chem. Phys.* 172, 98–104 (2016).

60. Thong PQ, Thu HPT, Huong LTT, Nguyen LH, Phuc NX. Structure and properties of Fe$_3$O$_4$ nanoparticles coated by PLA-PEG copolymer with and without loading of curcumin. *Vietnam J. Sci. Technol.* 54(1A), 268–276 (2016).

61. Kallumadil M, Tada M, Nakagawa T, Abe M, Southern P, Pankhurst QA. Suitability of commercial colloids for magnetic hyperthermia. *J. Magn. Magn. Mater.* 321(10), 1509–1513 (2009).

62. Faustino-Rocha A, Oliveira PA, Pinho-Oliveira J *et al.* Estimation of rat mammary tumor volume using caliper and ultrasonography measurements. *Lab Anim. (NY)* 42(6), 217–224 (2013).

63. Wang G, Zhang X, Skallberg A *et al.* One-step synthesis of water-dispersible ultra-small Fe$_3$O$_4$ nanoparticles as contrast agents for T1 and T2 magnetic resonance imaging. *Nanoscale* 6(5), 2953–2963 (2014).

64. Hachani R, Lowdell M, Birchall M, Thanh NTK. Tracking stem cells in tissue-engineered organs using magnetic nanoparticles. *Nanoscale* 5(23), 11362–11373 (2013).

65. Li W, Tutton S, Vu AT *et al.* First-pass contrast-enhanced magnetic resonance angiography in humans using ferumoxytol, a novel ultrasmall superparamagnetic iron oxide (USPIO)-based blood pool agent. *J. Magn. Reson. Imaging* 21(1), 46–52 (2005).

66. Dallet L, Stanicki D, Voisin P, Miraux S, Ribot EJ. Micron-sized iron oxide particles for both MRI cell tracking and magnetic fluid hyperthermia treatment. *Sci. Rep.* 11(1), 1–13 (2021).

67. Kossatz S, Ludwig R, Dähring H *et al.* High therapeutic efficiency of magnetic hyperthermia in xenograft models achieved with moderate temperature dosages in the tumor area. *Pharm. Res.* 31(12), 3274–3288 (2014).

68. Mamiya H. Recent advances in understanding magnetic nanoparticles in AC magnetic fields and optimal design for targeted hyperthermia. *J. Nanomater.* 2013, 752973 (2013).

69. Simeonidis K, Morales MP, Marciello M *et al.* In-situ particles reorientation during magnetic hyperthermia application: shape matters twice. *Sci. Rep.* 6, 1–11 (2016).

70. Storozhuk L, Besenhard MO, Mourdikoudis S *et al.* Stable iron oxide nanoflowers with exceptional magnetic heating 2 efficiency: simple and fast polyol synthesis. *ACS Appl. Mater. Interfaces* 13(38), 45870–45880 (2021).

71. Devkota J, Mai TTT, Stojak K *et al.* Synthesis, inductive heating, and magnetoimpedance-based detection of multifunctional Fe$_3$O$_4$ nanoconjugates. *Sensors Actuators, B Chem.* 190, 715–722 (2014).

72. Xiong XY, Tam KC, Gan LH. Release kinetics of hydrophobic and hydrophilic model drugs from pluronic F127/poly(lactic acid) nanoparticles. *J. Control. Rel.* 103(1), 73–82 (2005).

73. Mukhopadhyay A, Joshi N, Chattopadhyay K, De G. A facile synthesis of PEG-coated magnetite (Fe₃O₄) nanoparticles and their prevention of the reduction of cytochrome C. *ACS Appl. Mater. Interfaces* 4(1), 142–149 (2012).

74. Phan QT, Le MH, Le TTH, Tran THH, Xuan PN, Ha PT. Characteristics and cytotoxicity of folate-modified curcumin-loaded PLA-PEG micellar nano systems with various PLA:PEG ratios. *Int. J. Pharm.* 507(1–2), 32–40 (2016).

75. Rachmawati H, Yanda YL, Rahma A, Mase N. Curcumin-loaded PLA nanoparticles: formulation and physical evaluation. *Sci. Pharm.* 84(1), 191–202 (2016).

76. Kumaraswamy P, Sethuraman S, Krishnan UM. Mechanistic insights of curcumin interactions with the core-recognition motif of β-amyloid peptide. *J. Agric. Food Chem.* 61(13), 3278–3285 (2013).

77. Souza TGF, Ciminelli VST, Mohallem NDS. A comparison of TEM and DLS methods to characterize size distribution of ceramic nanoparticles. *J. Phys. Conf. Ser.* 733(1), 012039 (2016).

78. Wilson BK, Prud'homme RK. Nanoparticle size distribution quantification from transmission electron microscopy (TEM) of ruthenium tetroxide stained polymeric nanoparticles. *J. Colloid Interface Sci.* 604, 208–220 (2021).

79. Linh PH, Van Thach P, Tuan NA *et al.* Magnetic fluid based on Fe₃O₄ nanoparticles: preparation and hyperthermia application. *J. Phys. Conf. Ser.* 187, 012069 (2009).

80. Lima E, De Biasi E, Mansilla MV *et al.* Heat generation in agglomerated ferrite nanoparticles in an alternating magnetic field. *J. Phys. D. Appl. Phys.* 46(4), 045002 (2013).

81. Urtizberea A, Natividad E, Arizaga A, Castro M, Mediano A. Specific absorption rates and magnetic properties of ferrofluids with interaction effects at low concentrations. *J. Phys. Chem. C* 114(11), 4916–4922 (2010).

82. Dash A, Blasiak B, Tomanek B, van Veggel FCJM. Validation of inner, second, and outer sphere contributions to T1 and T2 relaxation in Gd³⁺-based nanoparticles using Eu³⁺ lifetime decay as a probe. *J. Phys. Chem. C* 122(21), 11557–11569 (2018).

83. Hobson NJ, Weng X, Ashford M, Thanh NTK, Schätzlein AG, Uchegbu IF. Facile aqueous, room temperature preparation of high transverse relaxivity clustered iron oxide nanoparticles. *Colloids Surfaces A Physicochem. Eng. Asp.* 570, 165–171 (2019).

•   **This article provides an easy way to prepare cluster Fe₃O₄ nanoparticles with high transverse relaxivity.**

84. Li H, Yan K, Shang Y *et al.* Folate-bovine serum albumin functionalized polymeric micelles loaded with superparamagnetic iron oxide nanoparticles for tumor targeting and magnetic resonance imaging. *Acta Biomater.* 15, 117–126 (2015).

85. Chen L, Wu Y, Wu H *et al.* Magnetic targeting combined with active targeting of dual-ligand iron oxide nanoprobes to promote the penetration depth in tumors for effective magnetic resonance imaging and hyperthermia. *Acta Biomater.* 96, 491–504 (2019).

86. Mai BT, Balakrishnan PB, Barthel MJ *et al.* Thermoresponsive iron oxide nanocubes for an effective clinical translation of magnetic hyperthermia and heat-mediated chemotherapy. *ACS Appl. Mater. Interfaces* 11, 5727–5739 (2019).

87. Moros M, Idiago-López J, Asín L *et al.* Triggering antitumoural drug release and gene expression by magnetic hyperthermia. *Adv. Drug Deliv. Rev.* 138, 326–343 (2019).

88. Liu JF, Jang B, Issadore D, Tsourkas A. Use of magnetic fields and nanoparticles to trigger drug release and improve tumor targeting. *Wiley Interdiscip. Rev. Nanomed. Nanobiotechnol.* 11(6), 1–29 (2019).

89. Wei Y, Quan L, Zhou C, Zhan Q. Factors relating to the biodistribution & clearance of nanoparticles & their effects on *in vivo* application. *Nanomedicine* 13(12), 1495–1512 (2018).

90. Pham HN, Ha T, Pham G *et al.* Magnetic inductive heating of organs of mouse models treated by copolymer. *Adv. Nat. Sci. Nanosci. Nanotechnol.* 8(025013), 1–10 (2017).

91. Alphandéry E. Perspectives of breast cancer thermotherapies. *J. Cancer* 5(6), 472–479 (2014).

92. Lee JH, Jang JT, Choi JS *et al.* Exchange-coupled magnetic nanoparticles for efficient heat induction. *Nat. Nanotechnol.* 6(7), 418–422 (2011).